Evaluation of the wind farm parameterization in the Weather Research and Forecasting model (version 3.8.1) with meteorological and turbine power data

Joseph C. Y. Lee and Julie K. Lundquist[1,2]

5 [1]Department of Atmospheric and Oceanic Sciences, University of Colorado, UCB 311, Boulder, CO 80309, USA
[2]National Renewable Energy Laboratory, Golden, CO, USA

Correspondence to: Joseph C. Y. Lee (chle6805@coloardo.edu)

Abstract. Forecasts of wind power production are necessary to facilitate the integration of wind energy into power grids, and these forecasts should incorporate the impact of wind turbine wakes. This paper focuses on a case study of four diurnal

10 cycles with significant power production, and assesses the skill of the wind farm parameterization (WFP) distributed with the Weather Research and Forecasting (WRF) model version 3.8.1, as well as its sensitivity to model configuration. After validating the simulated ambient flow with observations, we quantify the value of the WFP as it accounts for wake impacts on power production of downwind turbines. We also illustrate that a vertical grid with nominally 12-m vertical resolution is necessary for reproducing the observed power production, with statistical significance. Further, the WFP overestimates wake

15 effects and hence underestimates downwind power production during high wind speed and low turbulence conditions. We also find the WFP performance is independent of atmospheric stability, the number of wind turbines per model grid cell, and the upwind-downwind position of turbines. Rather, the ability of the WFP to predict power production is most dependent on the skill of the WRF model in simulating the ambient wind speed.

1 Introduction

20 In recent years, numerical weather prediction (NWP) models have become an indispensable tool in the wind energy industry, not only in day-to-day wind energy production forecasts (Wilczak et al., 2015), but also to support wide-scale wind power penetration (Marquis et al., 2011) and wind resource assessment. To forecast power production accurately at wind farms, the simulation tools should resolve all physical processes relevant to the wind field, including possible impacts of the wind turbines themselves. Consequently, including the effects of wind farms in NWP models can improve power production

25 forecasts.

Researchers have developed various methods to numerically represent wind farms. Via large-eddy simulations (LES), some investigators assess the meteorological impacts of wind turbines as well as power production (Abkar and Porté-Agel, 2015b; Aitken et al., 2014; Calaf et al., 2010; Churchfield et al., 2012; Jimenez et al., 2007; Mirocha et al., 2014; Na et al.,

2016; Sharma et al., 2016; Wu and Porté-Agel, 2011). Simulating wind turbines and their effects in LES is, while useful,
30   computationally expensive, making wind-farm-scale simulations unreasonable in an operational setting.

At coarser spatial scales, suitable for global, synoptic or mesoscale models, numerically representing wind turbine
effects may involve unrealistic assumptions. For example, researchers have used exaggerated surface roughness to represent
the wind speed (WS) reduction caused by wind farms in a global model (Barrie and Kirk-Davidoff, 2010; Frandsen et al.,
2009; Keith et al., 2004). Similarly, the analytical wind park model of Emeis and Frandsen (1993) considers both the
35   downward momentum flux and the momentum loss due to surface roughness, which are both dependent on atmospheric
stability (Emeis, 2010). However, these models omit the consideration of turbine-scale interactions between the hub and the
surface (Abkar and Porté-Agel, 2015a; Fitch et al., 2012, 2013b).

Aside from indirectly representing wind turbines via exaggerated roughness, another common approach is to use the
turbine power curve to deduce elevated drag and turbulence production of wind turbines. A power curve illustrates the
40   relationship between inflow WS at hub height and power production of a particular turbine model. This method can model
meteorological impacts of wind turbines and the impact of turbine drag force (Baidya Roy, 2011; Blahak et al., 2010). Based
on this technique, Fitch et al. (2012) added the consideration of the turbine thrust coefficient to simulate both turbine drag
and power loss.

In the wind farm parameterization (WFP) of the Weather Research and Forecasting (WRF) model, wind turbines in each
45   model grid cell are collectively represented as a turbulence source and a momentum sink within the vertical levels of the
turbine rotor disk (Fitch et al., 2012). A fraction of the kinetic energy extracted by the virtual wind turbines is converted to
power, and the turbulence generation is derived from the difference between the thrust and power coefficients. In the WFP
scheme, the use of the WS-dependent thrust coefficients accounts for the effects of local wind drag on wind energy
extraction as well as on power estimation. The WRF WFP offers flexibility, where users can modify the parameters of a
50   turbine model, such as its hub height, rotor diameter, power curve and thrust coefficients, and does not require other
empirically-derived parameters. By simulating wind farms in a mesoscale weather model, WRF users can simulate
aggregated effects of wind turbine wakes and thus the effects of power production of downwind turbines.

An approach similar to the WRF WFP proposed by Abkar and Porté-Agel (2015a), relies on an extra parameter, the
ratio of the freestream velocity to the horizontal averaged hub-height velocity of a turbine-containing grid cell. This ratio
55   depends on various factors such as the wind farm density and layout, and requires preliminary simulation results (Abkar and
Porté-Agel, 2015a). Therefore, the publicly-available WFP in the WRF model is chosen in this project for observed power
comparison. On the other hand, the explicit wake parameterization (WEP) recently designed by Volker et al. (2015) uses
classical wake theory to describe the unresolved wake expansion. Both the WRF WFP and the WEP average the drag force
within grid cells. Nevertheless, users of the WEP need to adjust the length scales that determine wake expansion in the WEP
60   for different situations.

In this paper, we evaluate the WFP in the WRF model via comparison to turbine power production data. The WRF WFP
has been widely used to assess the impacts, of both onshore and offshore wind farms, at different spatial scales, and in

different stability regimes (Eriksson et al., 2015; Fitch et al., 2013a, 2013b; Jiménez et al., 2015; Lee and Lundquist, 2017; Miller et al., 2015; Vanderwende et al., 2016; Vanderwende and Lundquist, 2016; Vautard et al., 2014). While WFP predictions have been compared to power production in offshore wind farms for a limited set of wind speeds (Jiménez et al., 2015), here we explore a range of WS, wind direction (WD), turbulence, and atmospheric stability conditions. The large range of wind conditions induces spatially- and temporally-diverse power production, thereby providing a basis for a comprehensive evaluation of the WFP. The uniqueness of this project lies in the in-depth assessment of the WRF WFP performance in forecasting and simulating wind energy of a sizable onshore wind farm, using observed power production data.

We describe the observation data and the model design in Section 2. In Section 3, we evaluate the simulations by comparison to meteorological and power generation data. We close with a statistical examination and a proposal of improvements on the WRF WFP in Section 4.

2 Data and Methods

2.1 Observations

The 2013 Crop Wind Energy eXperiment (CWEX-13) took place in central Iowa at a 200-turbine wind farm to quantify far-wake impacts of multiple rows of turbines (Lundquist et al., 2014). In CWEX-13, measurements from seven surface flux stations, a radiometer, three profiling lidars and a scanning lidar were collected. This campaign was a component of the larger CWEX project, which explored the interactions of wind turbines with crops, surface fluxes and near-surface flows in different atmospheric stability regimes in flat terrain (Rajewski et al., 2013). Research facilitated by the CWEX projects include: diurnal changes in observed turbine wakes (Rhodes and Lundquist, 2013), turbine interactions with moisture and carbon dioxide fluxes (Rajewski et al., 2014), LES modelling of turbine wakes in changing stability regimes (Mirocha et al., 2015), nocturnal low-level jet (LLJ) occurrences (Vanderwende et al., 2015), diurnal changes of the microclimate near wind turbines (Rajewski et al., 2016), multiple-wake interactions (Bodini et al., 2017), the evolution of turbine wakes during the evening transition (Lee and Lundquist, 2017) and coupled mesoscale-microscale modelling (Muñoz-Esparza et al., 2017).

This wind farm consists of 200 wind turbines, represented by the red dots in Fig. 1. Half of the wind turbines in the wind farm are General Electric (GE) 1.5-MW super-long extended (SLE) model, and the other half are GE 1.5-MW extra-long extended (XLE) model (Rajewski et al., 2013). The cut-in and cut-out speeds of the SLE model are 3.5 and 25 m s^{-1} respectively, and the rated speed is 14 m s^{-1}. The XLE model has lower rated and cut-out wind speeds, at 11.5 and 20 m s^{-1}. The hub height of both models is 80 m; the rotor diameters of the SLE and the XLE model are 77 and 82.5 m respectively. For simplicity, references to the rotor diameter (D) herein refer to the 77-m rotor diameter. Power generated by each turbine is recorded by the Supervisory Control and Data Acquisition (SCADA) system every 10 minutes, and we sum up the power production of all turbines for wind-farm production for each 10-min period.

95   Observations of the wind profile are collected by a profiling lidar and a scanning lidar. The WINDCUBE v1 (WC) profiling lidar (yellow square in Fig. 1), is located 528 m, or 6.3 D, south of the nearest turbine. The WC lidar measures winds at about 0.25 Hz from 40 to 220 m above ground level (AGL) every 20 m. The WC lidar derives wind components by measuring radial velocities using Doppler beam swinging at an azimuth angle of 28°. Note that the WC-observed turbulence parameters, turbulence kinetic energy (TKE) and turbulence intensity (TI), are derived from the variances of the three wind

100   components in two-min intervals, hence not representing small-scale turbulence. The turbulence parameters are defined by:

$$TKE = \frac{1}{2}(\sigma_u^2 + \sigma_v^2 + \sigma_w^2), \tag{1}$$

$$TI = \frac{\sqrt{\sigma_u^2 + \sigma_v^2}}{\overline{U}}, \tag{2}$$

where σ^2 are the 2-min averaged variances of the u, v, and w wind components, and $\overline{U}$ is the mean horizontal WS (Stull, 1988). In CWEX-11, wind turbine wake measurements at a different location in this wind farm were collected with these

105   instruments (Rhodes and Lundquist 2013), while the error in these lidar measurements due to inhomogeneous flow were explored by Bingöl et al. (2009) and Lundquist et al. (2015).

     The WINDCUBE 200S scanning lidar (green square in Fig. 1), is positioned 437 m, or 5.7 D, north of the nearest turbine row. The 200S lidar scanning strategy included velocity azimuth display (VAD) scans that measures winds from ~ 100 to ~ 4800 m AGL nominally every 50 m. We use the 200S 75-degree-elevation scans (Vanderwende et al., 2015) to

110   estimate horizontal winds every 30 minutes to verify the simulated winds in the boundary layer. Since the dominant wind directions during the campaign are southerly and south-westerly (Vanderwende et al., 2015), a majority of the 200S measurements below the rotor top (about 120 m AGL) could be influenced by turbine wakes during conditions, in which wakes persist longer than 5 D downwind from the turbine.

     Surface flux station measurements can also quantify model skill. The surface flux station of interest (purple square in

115   Fig. 1), is located 681 m, or 8.8 D, south of the closest turbine. At 8 m AGL, the station measures 20-Hz winds via a CSAT3 sonic anemometer, as well as virtual temperature and water vapour density via a HMP45C probe. After tilt-correction (Wilczak et al., 2001), we calculate sensible heat flux using a 30-min averaging time period. The Obhukov length (L) categorizes atmospheric stability conditions:

$$L = -\frac{\overline{T_v}u_*^3}{kg(\overline{w'T_v'})_s}, \tag{3}$$

120   where $\overline{T_v}$ is the mean virtual temperature, u_* is the frictional velocity, k is the von Karman constant, g is the gravity acceleration, and $(\overline{w'T_v'})_s$ is the surface virtual temperature flux calculated from the 20-Hz measurements (Stull, 1988). A positive Obukhov Length ratio ($z L^{-1}$), where z is 8 m, indicates a stable atmosphere, while a negative value indicates unstable conditions.

     From 24-27 August 2013, nocturnal LLJs were observed (Vanderwende et al., 2015). No major synoptic events

125   affected the area during this period. Moreover, when the near-surface flows are southerly, the WC and the surface flux station measure winds unaffected by the presence of wind turbines (Muñoz-Esparza et al., 2017). Additionally, no

curtailment of the wind turbines occurred and the instruments operated normally during the period, making these four days ideal for model verification.

2.2 Modelling

130   To establish direct comparison with the observations, we simulate winds with and without the wind farm parameterization (WFP) using the Advanced Research WRF model (version 3.8.1) (Skamarock and Klemp, 2008). We simulate the winds on each day separately, from 0 UTC to 0 UTC, after 12 h of spin-up time. The ERA-interim (Dee et al., 2011) and the 0.5° Global Forecast System (GFS) reanalysis datasets provide boundary conditions for two different sets of model runs. We set three domains in our simulations with horizontal resolutions of 9, 3 and 1 km respectively, where the

135   finest domain covers the state of Iowa (Fig. 1). To capture the westerly synoptic flow and the southerly near-surface winds, we position the inner grids northeast of the centres of the coarser grids.

We employ two resolutions of vertical grids: nominally 12 m and 22 m resolution below 400 m above the surface, with 80 and 70 total levels respectively (Fig. 2). Three and six vertical levels intersect the atmosphere below and within the rotor layer in the finer vertical grid, while the 22-m grid only allows one full level below and four levels within the rotor layer.

140   The vertical levels are further stretched beyond the boundary layer. In past research involving the WRF WFP, the selections of vertical resolution within the rotor layer include: 9 to 18 m in Vanderwende et al. (2016); about 10 to 16 m in Volker et al. (2015); about 15 m in Fitch et al. (2012), Fitch et al. (2013a), Fitch et al. (2013b) and Vanderwende and Lundquist (2016); about 20 m in Miller et al. (2015) and Vautard et al. (2014); about 22 m in Lee and Lundquist (2017); about 40 m in Eriksson et al. (2015) and Jiménez et al. (2015).

145   The Mellor-Yamada-Nakanishi-Niino (MYNN) Level 2.5 Planetary Boundary Layer (PBL) scheme is currently required for use with the WFP distributed with the WRF model version 3.8.1 (Fitch et al., 2012). Note that substantial upgrades were made on the MYNN PBL schemes in WRF version 3.8 (WRF-ARW, 2016). The MYNN PBL scheme supports TKE advection, active coupling to radiation, cloud mixing from Ito et al. (2015) and mixing of scalar fields. The MYNN scheme also uses the cloud probability density function from Chaboureau and Bechtold (2002), and we keep the

150   mass-flux scheme deactivated. We summarize the other configuration details in Table 1.

After verifying the background flow simulated by the WRF model (first 4 rows in Table 2), virtual turbines are added via the WFP (last 4 rows in Table 2). We simulate all the turbines using the 1.5-MW PSU generic turbine model (Schmitz, 2012), in which its specifications are based on the GE 1.5-MW SLE model installed at the wind farm. The turbines within the WRF grid cells are located with the latitudes and longitudes provided by the wind-farm owner-operator. The model grid

155   cells within the wind farm, containing 1 to 4 wind turbines per cell, are labelled as blue numbers in Fig. 1. With the WFP activated, the model simulates the total power at each time step in each turbine-containing grid cell, regardless of the number of turbines per cell. To match the 10-min average power data from the turbines, we sample 10-min power from the WFP output.

We also estimate the power generation of the WRF simulations without using the WFP. Based on the ambient WS of
160   the turbine-containing grid cells in the control WRF runs, we use the turbine power curve to obtain an assessment of the
power every ten minutes. We then multiply the power with the number of turbines per cell to yield the appropriate power
estimate in each grid cell, just as would be done in wind energy forecasting without a wake parameterization. This method of
power estimation omits wake effects, in contrast to the WFP.

3 Results

165   ### 3.1 Ambient Flow Evaluation

The WRF model simulations without the WFP simulate accurate ambient winds as compared to the lidar
measurements. Qualitatively, the ERA12 simulation (see Table 2 for a listing of all the simulations), has skill in simulating
WS and WD during the 4-day period, including the occurrence, the strength and the elevation of the nocturnal low-level jets
(Fig. 3). Except for the last hours on 24 August, the ERA12 captures the general temporal and vertical fluctuations in WS
170   and WD, as the winds changed from south-easterly to south-westerly (Fig. 3 and 4). To evaluate the effects of boundary
conditions and vertical resolutions on simulating winds, we compare the 4 no-WFP runs: ERA12, ERA22, GFS12 and
GFS22.

Quantitatively, simulations using finer vertical resolution have more skill in simulating winds than those with coarser
resolution (Table 3). In comparison to the 200S and WC observations, the mean absolute errors in WS and WD of the 12-m
175   runs are lower than those of the 22-m runs over the 4-day period, by 0.3 m s^{-1} and 0.8° in average. Particularly in the ERA12,
the errors in WS decrease by at least 19% relative to the ERA22. Although the GFS22 yields smaller WS errors than the
ERA22, refining the vertical grid of the simulations of either boundary condition dataset improves the skill of the WRF
model more than changing the boundary conditions (Table 3). The errors in simulating WD remain similar regardless of the
choice of boundary condition or vertical grid. Of all our control runs, the ERA12 simulates the most accurate inflow.

180   ### 3.2 Power Simulations

The simulation omitting the WFP ignores the wake effects on downwind turbine power production, and therefore
overestimates total power. For each 10-min time step, we compare the spatial distribution of power production as well as the
total power between the ERA12, the ERA12WF, and the observations; Fig. 5 represents one 10-min time step in the 4-day
period. As mentioned above, we calculate the power estimates of ERA12 using the ambient WS and the number of turbines
185   in each grid cell as well as the power curve (Fig. 5a). The WRF WFP generates power predictions (Fig. 5b), and we sum up
the observed power production in each grid cell (Fig. 5c). We present the total 10-min observed and simulated power of the
whole wind farm at the bottom of each panel in Fig. 5. We then compile the 576 10-min total power values over the 4-day
period and compare the simulations to the observations (Fig. 6). We also calculate an error and a bias of modelled total

power for each 10-min interval, summarizing as the daily root-mean-squared errors (RMSE) and average biases in Table 4
190   and 5. The large average biases in Table 5 highlight the consistent power overestimation of the no-WFP runs.

Over the 4-day period, the WFP produces total power of the whole wind farm that generally agrees with observation
(Fig. 6c). Although the RMSEs between the no-WFP and WFP runs are comparable (Table 4), the average biases are smaller
in the WFP simulations (Table 5). For example, the ERA12WF slightly under-predicts total power by -4.9 MW on average
(Fig. 6c and Table 5). The ERA12, by contrast, consistently over-predicts power production by 41.5 MW (Fig. 6a and Table
195   5). The daily positive biases of the ERA12 in the first 2 days are nearly 20% of maximum wind farm production (Table 5).
The average positive power bias of 36.2 MW in the ERA22 is also remarkably larger than the mild negative bias of -15.1
MW in the ERA22WF (Fig. 6b and d, Table 5). Furthermore, the ERA12 and the GFS12 generally outperform the ERA22
and the GFS22 in power predictions, particularly in RMSE (Fig. 6 and Table 5). However, on the last day, with more south-
westerly flow, the ERA12 and the ERA22 outperform the ERA12WF and the ERA22WF, while the GFS12WF and the
200   GFS22WF yield smaller errors and biases (Table 4 and 5). Nonetheless, in aggregate, the simulations using the WFP predict
wind-farm power production with more skill than simulations without the WFP.

As demonstrated by the average absolute errors (Table 3), the WFP power simulations improve when using 12-m rather
than 22-m vertical resolution (Fig. 6). Changing the vertical grid improves the predictions more than changing boundary
conditions (Table 4 and 5). Particularly in the ERA-interim simulations, the RMSE each day decreases by 19% to 39% when
205   switching from ERA22WF to ERA12WF, also seen in Fig. 6c and d. Since the power prediction skills of the ERA-interim-
initiated runs and the GFS-initiated runs are comparable, the rest of the paper will focus on the WFP runs using the ERA-
interim initial and boundary conditions.

Given the utility of the WFP, assessing the interactions between atmospheric forcing and power is an important step to
further examine the performance of the WFP. As with the ERA12, the ERA12WF adequately simulates the evolution of the
210   meteorological variables over the 4-day period (Fig. 7a to c). Both the ERA12 and the ERA12WF capture the overall trends
of hub-height ambient WS and WD (Fig. 7a and b), corresponding to Fig. 3 and 4. On the other hand, although the
simulations suggest stronger TKE diurnal cycles than the observations, especially in the first 36 h, the simulated values
follow the trends of the WC-measured TKE (Fig. 7c).

The observed WS fluctuates more than the mesoscale simulated WS during daytime (Fig. 7a). The ramp events, where
215   the WS increases rapidly in a short period (Kamath, 2010; Potter et al., 2009), induce considerable increases in observed
power (Fig. 7d). The five distinct ramp events are from 00 to 01 UTC on 24 August, from 18 to 19 UTC 24 August, from 00
to 01 UTC 25 August, from 00 to 02 UTC 26 August, and from 00 to 02 UTC 27 August. Most of the ramp events are
related to the LLJs (Fig. 3), and the simulated WS usually lags that observed (Fig. 7a). Therefore, the WFP under-predicts
total power in nearly all the ramp events (Fig. 7d). Note that the measured WS ranges between the cut-in and rated speed of
220   the wind turbine, a range in which the power is highly sensitive to WS. The strong linkage between the temporal fluctuations
of WS and power emphasizes the importance of accurate WS predictions.

Along the same line, the WFP power performance changes in different meteorological conditions. To quantify WFP's skills, we use the bias in total power as a benchmark, calculated by subtracting the observed power from the WFP simulated power every 10 minutes (Fig. 8). Particularly in conditions of strong winds and weak turbulence, the WFP overestimates

225 wake effects and thus underestimates power. On the other hand, for calm conditions with moderate or strong turbulence, the WFP tends to underestimate wake effects and thereby over-predicts power (Fig. 8a and c). The Pearson correlation coefficient between total power bias and WC-observed TKE is 0.48 (not shown).

On the contrary, WD and atmospheric stability have weaker influence on the skill of the WFP. The winds gradually rotate from south-easterly to south-westerly over this 4-day period while maintaining similar magnitudes of wind speed.

230 During this direction shift, the WFP demonstrates a weak positive power bias when the WD is strictly southerly, while the biases skew negative when the winds have more easterly or westerly component (Fig. 8b). Similarly, the WFP power bias is unresponsive to stability changes, although strongly stable conditions tend to have low bias (Fig. 8d). At the same time, strongly stable conditions tend to have stronger and more distinct wakes (Abkar and Porté-Agel, 2015b; Lee and Lundquist, 2017; Magnusson and Smedman, 1994; Rhodes and Lundquist, 2013).

235 As may be expected, when the model properly simulates ambient WS, the WFP performs better. When the ERA12WF predicts larger WS than observed, the simulation over-predicts the total power. The positive WFP power bias corresponds to WS overestimation, and the negative bias is associated with WS underestimation (Fig. 9). Interestingly, when the error in simulated total power lies between ± 30 MW, the error of the simulated WS is mostly within ± 2 m s^{-1}. On the other hand, the power bias does not seem to be related to wind direction or to ambient TKE: the correlation between the power bias and the

240 simulated WD (TKE) bias is low, 0.3 (0.22) (not shown). Although the simulated WD and TKE generally match the WC observations (Fig. 7b and c), and the model's skills in simulating WD and TKE are relatively irrelevant to the WFP's power performance.

Although the WFP omits sub-grid-scale wake interactions between the wakes of multiple turbines within a cell, this omission does not affect the accuracy of the ERA12WF in power prediction: the performance of the WFP is insensitive to

245 the number of turbines per model grid cell. The turbine-normalized bias demonstrates no dependence on the number of turbines within the model grid cell (Fig. 10). Each whisker in Fig. 10 marks the maximum, the upper quartile, the median, the lower quartile and the minimum of the average bias. Despite the large positive biases of the maxima, more than half of the average biases fall between ± 1.5 MW, regardless of the numbers of turbines per cell (Fig. 10). Simulating 1 or 4 turbines in a grid cell (Fig. 1) does not influence the WFP's overall power prediction performance in the cases shown here.

250 **4 Discussion**

Herein, we compare WRF model simulations with different choices of vertical resolutions and boundary conditions. The evidence suggests that, at least for this onshore case with a strong diurnal cycle, the vertical resolution is more crucial than the choice of boundary conditions in simulating accurate winds and wind power production. Shin et al. (2011) have

explored the impacts of the lowest model level on the performance of various PBL schemes in the WRF model, suggesting
that increasing the number of model layers can simulate more accurately the surface layer in different stability regimes. In
this study, we further illustrate that establishing more vertical levels in the boundary layer as well as the rotor layer improves
the skills of the WRF model in simulating ambient WS, ambient WD and wind power (Table 3, 4 and 5). Furthermore,
Carvalho et al. (2014) discussed the effects of different reanalysis datasets on wind energy production estimates and found
the ERA-interim presents the most precise initial and boundary conditions, followed by the GFS. Herein, we test the ERA-
interim and the 0.5° GFS, and both datasets produce simulations that resemble observed winds and power generations. Since
the simulated power is sensitive to the resolution of model vertical grid, particularly near the surface, future WRF WFP users
should select vertical levels with care.

Additionally, the outcomes from the statistical tests among the model runs further validate the importance of using the
WFP as well as using a fine vertical grid. From the Student's t-test, the p-values of all the no-WFP and WFP pairs are 0
(Table 6 and 7), demonstrating that the differences between the distributions of the no-WFP runs and the WFP runs are
statistically significant at any confidence level. Therefore, to accurately simulate power production, applying the WFP is
better than not using it, regardless of the choice of vertical resolution and boundary condition, and the corresponding
improvements in Table 4 and 5 are statistically significant. Although the distinction between the GFS12WF and GFS22WF
is not statistically significant at the 90% confidence level (Table 7), switching from ERA22WF to ERA10WF improves
power simulations significantly with 99% confidence (Table 6). In particular, the RMSE drops by 19.1 MW and the bias
reduces by 10.2 MW in average in the ERA12WF (Table 4 and 5), and these are proven statistically significant.

Similarly, results from the statistical tests between the distributions of power from models and observations support the
value of the WFP applied in a fine vertical grid. The p-values of the ERA12WF-observed pair and the GFS12WF-observed
pair are 0.106 and 0.167 respectively (Table 8). The high p-values illustrate the distinctions between the distribution of
observed power and the distributions of simulated power from the 12-m WFP simulations are not statistically significant, at
the 90% confidence level. Among all the simulations analysed above, running the WFP over the 12-m vertical grid is the
only combination that is not statistically different from observations (Table 8). In other words, the 12-m WFP simulations
provide the closest approximations, of all the simulations, to the actual power production. Hence, the only way to predict
wind-farm power production using the WRF model that is similar to (not statistically different from) observations is to use
the WFP with 12-m resolution, regardless of the boundary condition dataset.

One of the objectives of this study is to propose general directions for improvements on the WFP. First of all, as the
key determining factor in wind power production, WS plays a critical role. Ramp events pose a challenge to the WRF model
in simulating WS as well as to the WFP in predicting power (Fig. 7a and d). On the other hand, wind speeds exceeding 10 m
s^{-1}, although below rated speed, lead to WFP power underestimation (Fig. 8a). Furthermore, the WFP performance depends
more on the horizontal winds and turbulence, rather than their vertical components, since the power bias correlates stronger
with TI than TKE (Fig. 8). More importantly, improving the skills of the WRF model in simulating WS can improve the

WFP power performance (Fig. 9). Future versions of the WRF model as well as the WFP should aim to better account for instantaneous horizontal WS variations and the subsequent sub-gird wake interactions.

In contrast, WD has no clear influence on the WFP skill (Fig. 8b) in this case, although the irregular shape of the wind

290   farm adds uncertainty to this relationship. Similarly, the skill of the WFP for this case is insensitive to atmospheric stability, the number of virtual turbines per cell, and the downwind position of turbines against inflow (Fig. 8d, 10 and 11). Compared to the power overestimation of downwind turbines in the idealized cases described in Vanderwende et al. (2016), both the upwind and downwind turbine-containing cells presented in this study have consistent positive biases on power production (Fig. 11). Our findings suggest that the WFP is skilful in simulating power of aggregate wind turbines and can represent the

295   impact of wakes between grids on power. In the end, the primary limitation of the WFP is rooted in the ambient simulated WS in the WRF model.

5 Conclusion

The WFP scheme in the WRF model (version 3.8.1) provides a convenient way to represent wind farms and their meteorological impacts in the NWP models. However, its power predictions have not been verified for onshore wind farms

300   or in a range of wind speed conditions. Herein, we evaluate the performance of the WFP in a range of atmospheric conditions to guide users of the WFP and to suggest future WFP advancements.

Using data from the CWEX-13 campaign, we select a 4-day period, from 24 to 27 August 2013, for our case study, due to the consistent nocturnal low-level jet occurrences. We use measurements from a profiling lidar, a scanning lidar and a surface flux station to verify the ambient flows simulated by the WRF model. The wind farm of interest, located in central

305   Iowa, consists of 200 1.5 MW wind turbines.

We explore the role of vertical resolution in the operation of the WRF WFP. We evaluate two vertical grids with 12-m and 22-m resolution near the surface. We find that the finer vertical resolution produces simulations that agree better with observed WS, WD and power than simulations with coarser vertical resolution. Further, because the WFP accounts for the impacts of wakes on downwind turbine power production, the use of the WFP enables more accurate power prediction,

310   whereas simulations without the WFP generally over-predict power production. Statically, the WFP simulations with a fine vertical grid, regardless of the boundary conditions, are the most skilful in simulating power.

The skill of the WFP varies with meteorological conditions. When the model simulates WS close to the observations, the WFP predicts power properly, making WS the critical factor in improving the WFP. Rapid temporal fluctuations in WS introduce errors in power simulations, especially during ramp events. Further, in windy and less turbulent conditions, the

315   WFP tends to overestimate wake effects and thus underestimates power production. On the other hand, the WFP performance demonstrates no clear dependence on atmospheric stability, the number of turbines per model grid cell, or the downwind distance of turbines with respect to the upwind ones.

In conclusion, we demonstrate the value of the WRF WFP and the importance of using a fine vertical grid. Since WS greatly affects the skill of the WFP, subsequent research could include evaluating the WFP for an even larger range of WS,
320 especially at wind speeds beyond the turbine cut-out speed (which would be 25 m s^{-1} in this case; no such high wind speeds were observed during the CWEX-13 campaign). Evaluating the performance of other wind farm layouts and in locations with complex terrain is also needed. Modifications in the inflow WS considered by the WFP, for example, considering the rotor equivalent wind speed (REWS) (Wagner et al., 2009), may bring promising improvements. More accurate power forecasts will shape a more competitive the wind energy industry, and further facilitate grid integration of wind energy
325 (MacDonald et al., 2016).

Data Availability

The PSU generic 1.5 MW turbine (Schmitz, 2012) is available at doi:10.13140/RG.2.2.22492.18567. The user input required to run the WRF WFP is available at doi:10.5281/zenodo.437166.

Acknowledgements

330 This study was funded by the National Science Foundation (Grant number: 1413980; Project Title: CNH-Ex: Legal, Economic, and Natural Science Analyses of Wind Plant Impacts and Interactions). The CWEX project was supported by the National Science Foundation under the State of Iowa EPSCoR Grant 1101284. The authors would like to acknowledge high-performance computing support from Yellowstone (ark:/85065/d7wd3xhc) provided by NCAR's Computational and Information Systems Laboratory, sponsored by the National Science Foundation. The authors would also like to thank
335 NextEra Energy for providing the wind turbine power data, Iowa State University for providing the surface flux measurements, and NRG Systems and Leosphere for providing the 200S scanning lidar used in the CWEX-13 campaign.

References

Abkar, M. and Porté-Agel, F.: A new wind-farm parameterization for large-scale atmospheric models, J. Renew. Sustain. Energy, 7(1), 13121, doi:10.1063/1.4907600, 2015a.
340 Abkar, M. and Porté-Agel, F.: Influence of atmospheric stability on wind-turbine wakes: A large-eddy simulation study, Phys. Fluids, 27(3), 35104, doi:10.1063/1.4913695, 2015b.
Aitken, M. L., Kosović, B., Mirocha, J. D. and Lundquist, J. K.: Large eddy simulation of wind turbine wake dynamics in the stable boundary layer using the Weather Research and Forecasting Model, J. Renew. Sustain. Energy, 6(3), 33137, doi:10.1063/1.4885111, 2014.
345 Baidya Roy, S.: Simulating impacts of wind farms on local hydrometeorology, J. Wind Eng. Ind. Aerodyn., 99(4), 491–498, doi:10.1016/j.jweia.2010.12.013, 2011.

Barrie, D. B. and Kirk-Davidoff, D. B.: Weather response to a large wind turbine array, Atmos. Chem. Phys., 10(2), 769–775, doi:10.5194/acp-10-769-2010, 2010.

Bingöl, F., Mann, J. and Foussekis, D.: Conically scanning lidar error in complex terrain, Meteorol. Zeitschrift, 18(2), 189–195, doi:10.1127/0941-2948/2009/0368, 2009.

Blahak, U., Goretzki, B. and Meis, J.: A simple parametrisation of drag forces induced by large wind farms for numerical weather prediction models, in EWEC, pp. 186–189, Proceedings European Wind Energy Conference and Exhibition., 2010.

Bodini, N., Zardi, D. and Lundquist, J. K.: Three-Dimensional Structure of Wind Turbine Wakes as Measured by Scanning Lidar, Atmos. Meas. Tech. Discuss., 1–21, doi:10.5194/amt-2017-86, 2017.

Calaf, M., Meneveau, C. and Meyers, J.: Large eddy simulation study of fully developed wind-turbine array boundary layers, Phys. Fluids, 22(1), 15110, doi:10.1063/1.3291077, 2010.

Carvalho, D., Rocha, A., Gómez-Gesteira, M. and Silva Santos, C.: WRF wind simulation and wind energy production estimates forced by different reanalyses: Comparison with observed data for Portugal, Appl. Energy, 117, 116–126, doi:10.1016/j.apenergy.2013.12.001, 2014.

Chaboureau, J.-P. and Bechtold, P.: A Simple Cloud Parameterization Derived from Cloud Resolving Model Data: Diagnostic and Prognostic Applications, J. Atmos. Sci., 59(15), 2362–2372, doi:10.1175/1520-0469(2002)059<2362:ASCPDF>2.0.CO;2, 2002.

Chen, F. and Zhang, Y.: On the coupling strength between the land surface and the atmosphere: From viewpoint of surface exchange coefficients, Geophys. Res. Lett., 36(10), L10404, doi:10.1029/2009GL037980, 2009.

Churchfield, M. J., Lee, S., Michalakes, J. and Moriarty, P. J.: A numerical study of the effects of atmospheric and wake turbulence on wind turbine dynamics, J. Turbul., 13, N14, doi:10.1080/14685248.2012.668191, 2012.

Dee, D. P., Uppala, S. M., Simmons, A. J., Berrisford, P., Poli, P., Kobayashi, S., Andrae, U., Balmaseda, M. A., Balsamo, G., Bauer, P., Bechtold, P., Beljaars, A. C. M., van de Berg, L., Bidlot, J., Bormann, N., Delsol, C., Dragani, R., Fuentes, M., Geer, A. J., Haimberger, L., Healy, S. B., Hersbach, H., Hólm, E. V, Isaksen, L., Kållberg, P., Köhler, M., Matricardi, M., McNally, A. P., Monge-Sanz, B. M., Morcrette, J.-J., Park, B.-K., Peubey, C., de Rosnay, P., Tavolato, C., Thépaut, J.-N. and Vitart, F.: The ERA-Interim reanalysis: configuration and performance of the data assimilation system, Q. J. R. Meteorol. Soc., 137(656), 553–597, doi:10.1002/qj.828, 2011.

Ek, M. B., Mitchell, K. E., Lin, Y., Rogers, E., Grunmann, P., Koren, V., Gayno, G. and Tarpley, J. D.: Implementation of Noah land surface model advances in the National Centers for Environmental Prediction operational mesoscale Eta model, J. Geophys. Res., 108(D22), 8851, doi:10.1029/2002JD003296, 2003.

Emeis, S.: A simple analytical wind park model considering atmospheric stability, Wind Energy, 13(5), 459–469, doi:10.1002/we.367, 2010.

Emeis, S. and Frandsen, S.: Reduction of horizontal wind speed in a boundary layer with obstacles, Boundary-Layer Meteorol., 64(3), 297–305, doi:10.1007/BF00708968, 1993.

Eriksson, O., Lindvall, J., Breton, S.-P. and Ivanell, S.: Wake downstream of the Lillgrund wind farm - A Comparison

between LES using the actuator disc method and a Wind farm Parametrization in WRF, J. Phys. Conf. Ser., 625(1), 12028, doi:10.1088/1742-6596/625/1/012028, 2015.

Fitch, A. C., Olson, J. B., Lundquist, J. K., Dudhia, J., Gupta, A. K., Michalakes, J. and Barstad, I.: Local and Mesoscale Impacts of Wind Farms as Parameterized in a Mesoscale NWP Model, Mon. Weather Rev., 140(9), 3017–3038, doi:10.1175/MWR-D-11-00352.1, 2012.

Fitch, A. C., Lundquist, J. K. and Olson, J. B.: Mesoscale Influences of Wind Farms throughout a Diurnal Cycle, Mon. Weather Rev., 141(7), 2173–2198, doi:10.1175/MWR-D-12-00185.1, 2013a.

Fitch, A. C., Olson, J. B. and Lundquist, J. K.: Parameterization of Wind Farms in Climate Models, J. Clim., 26(17), 6439–6458, doi:10.1175/JCLI-D-12-00376.1, 2013b.

Frandsen, S. T., Jørgensen, H. E., Barthelmie, R., Rathmann, O., Badger, J., Hansen, K., Ott, S., Rethore, P.-E., Larsen, S. E. and Jensen, L. E.: The making of a second-generation wind farm efficiency model complex, Wind Energy, 12(5), 445–458, doi:10.1002/we.351, 2009.

Iacono, M. J., Delamere, J. S., Mlawer, E. J., Shephard, M. W., Clough, S. A. and Collins, W. D.: Radiative forcing by long-lived greenhouse gases: Calculations with the AER radiative transfer models, J. Geophys. Res. Atmos., 113(D13), D13103, doi:10.1029/2008JD009944, 2008.

Ito, J., Niino, H., Nakanishi, M. and Moeng, C.-H.: An Extension of the Mellor–Yamada Model to the Terra Incognita Zone for Dry Convective Mixed Layers in the Free Convection Regime, Boundary-Layer Meteorol., 157(1), 23–43, doi:10.1007/s10546-015-0045-5, 2015.

Jimenez, A., Crespo, A., Migoya, E. and Garcia, J.: Advances in large-eddy simulation of a wind turbine wake, J. Phys. Conf. Ser., 75(1), 12041, doi:10.1088/1742-6596/75/1/012041, 2007.

Jiménez, P. A., Navarro, J., Palomares, A. M. and Dudhia, J.: Mesoscale modeling of offshore wind turbine wakes at the wind farm resolving scale: a composite-based analysis with the Weather Research and Forecasting model over Horns Rev, Wind Energy, 18(3), 559–566, doi:10.1002/we.1708, 2015.

Kain, J. S.: The Kain–Fritsch Convective Parameterization: An Update, J. Appl. Meteorol., 43(1), 170–181, doi:10.1175/1520-0450(2004)043<0170:TKCPAU>2.0.CO;2, 2004.

Kamath, C.: Understanding wind ramp events through analysis of historical data, in IEEE PES T&D 2010, pp. 1–6, IEEE., 2010.

Keith, D. W., DeCarolis, J. F., Denkenberger, D. C., Lenschow, D. H., Malyshev, S. L., Pacala, S. and Rasch, P. J.: The influence of large-scale wind power on global climate, Proc. Natl. Acad. Sci. U. S. A., 101(46), 16115–16120, doi:10.1073/pnas.0406930101, 2004.

Lee, J. C. Y. and Lundquist, J. K.: Observing and Simulating Wind-Turbine Wakes During the Evening Transition, Boundary-Layer Meteorol., Accepted, 2017.

Lundquist, J. K., Takle, E. S., Boquet, M., Kosović, B., Rhodes, M. E., Rajewski, D., Doorenbos, R., Irvin, S., Aitken, M. L., Friedrich, K., Quelet, P. T., Rana, J., Martin, C. S., Vanderwende, B. and Worsnop, R.: Lidar observations of interacting

415   wind turbine wakes in an onshore wind farm, in EWEA. [online] Available from: http://www.leosphere.com/wp-content/uploads/2014/03/Lundquist_Boquet_EWEA_2014_CWEX13_final.pdf (Accessed 10 May 2017), 2014.

Lundquist, J. K., Churchfield, M. J., Lee, S. and Clifton, A.: Quantifying error of lidar and sodar Doppler beam swinging measurements of wind turbine wakes using computational fluid dynamics, Atmos. Meas. Tech., 8(2), 907–920, doi:10.5194/amt-8-907-2015, 2015.

420   MacDonald, A. E., Clack, C. T. M., Alexander, A., Dunbar, A., Wilczak, J. and Xie, Y.: Future cost-competitive electricity systems and their impact on US CO2 emissions, Nat. Clim. Chang., 6(5), 526–531, doi:10.1038/nclimate2921, 2016.

Magnusson, M. and Smedman, A. S.: Influence of atmospheric stability on wind turbine wakes, Wind Eng., 18(3), 139–152, 1994.

Marquis, M., Wilczak, J., Ahlstrom, M., Sharp, J., Stern, A., Smith, J. C. and Calvert, S.: Forecasting the Wind to Reach
425   Significant Penetration Levels of Wind Energy, Bull. Am. Meteorol. Soc., 92(9), 1159–1171, doi:10.1175/2011BAMS3033.1, 2011.

Miller, L. M., Brunsell, N. A., Mechem, D. B., Gans, F., Monaghan, A. J., Vautard, R., Keith, D. W. and Kleidon, A.: Two methods for estimating limits to large-scale wind power generation, Proc. Natl. Acad. Sci., 112(36), 11169–11174, doi:10.1073/pnas.1408251112, 2015.

430   Mirocha, J. D., Kosovic, B., Aitken, M. L. and Lundquist, J. K.: Implementation of a generalized actuator disk wind turbine model into the weather research and forecasting model for large-eddy simulation applications, J. Renew. Sustain. Energy, 6(1), 13104, doi:10.1063/1.4861061, 2014.

Mirocha, J. D., Rajewski, D. A., Marjanovic, N., Lundquist, J. K., Kosović, B., Draxl, C. and Churchfield, M. J.: Investigating wind turbine impacts on near-wake flow using profiling lidar data and large-eddy simulations with an actuator
435   disk model, J. Renew. Sustain. Energy, 7(4), 43143, doi:10.1063/1.4928873, 2015.

Muñoz-Esparza, D., Lundquist, J. K., Sauer, J. A., Kosović, B. and Linn, R. R.: Coupled mesoscale-LES modeling of a diurnal cycle during the CWEX-13 field campaign: From weather to boundary-layer eddies, J. Adv. Model. Earth Syst., doi:10.1002/2017MS000960, 2017.

Na, J. S., Koo, E., Muñoz-Esparza, D., Jin, E. K., Linn, R. and Lee, J. S.: Turbulent kinetics of a large wind farm and their
440   impact in the neutral boundary layer, Energy, 95, 79–90, doi:10.1016/j.energy.2015.11.040, 2016.

Nakanishi, M. and Niino, H.: An Improved Mellor–Yamada Level-3 Model: Its Numerical Stability and Application to a Regional Prediction of Advection Fog, Boundary-Layer Meteorol., 119(2), 397–407, doi:10.1007/s10546-005-9030-8, 2006.

Potter, C. W., Grimit, E. and Nijssen, B.: Potential benefits of a dedicated probabilistic rapid ramp event forecast tool, in 2009 IEEE/PES Power Systems Conference and Exposition, pp. 1–5, IEEE., 2009.

445   Rajewski, D. A., Takle, E. S., Lundquist, J. K., Oncley, S., Prueger, J. H., Horst, T. W., Rhodes, M. E., Pfeiffer, R., Hatfield, J. L., Spoth, K. K. and Doorenbos, R. K.: Crop Wind Energy Experiment (CWEX): Observations of Surface-Layer, Boundary Layer, and Mesoscale Interactions with a Wind Farm, Bull. Am. Meteorol. Soc., 94(5), 655–672, doi:10.1175/BAMS-D-11-00240.1, 2013.

Rajewski, D. A., Takle, E. S., Lundquist, J. K., Prueger, J. H., Pfeiffer, R. L., Hatfield, J. L., Spoth, K. K. and Doorenbos, R.

450   K.: Changes in fluxes of heat, H2O, and CO2 caused by a large wind farm, Agric. For. Meteorol., 194, 175–187, doi:10.1016/j.agrformet.2014.03.023, 2014.

Rajewski, D. A., Takle, E. S., Prueger, J. H. and Doorenbos, R. K.: Toward understanding the physical link between turbines and microclimate impacts from in situ measurements in a large wind farm, J. Geophys. Res. Atmos., 121(22), 2016JD025297, doi:10.1002/2016JD025297, 2016.

455   Rhodes, M. E. and Lundquist, J. K.: The Effect of Wind-Turbine Wakes on Summertime US Midwest Atmospheric Wind Profiles as Observed with Ground-Based Doppler Lidar, Boundary-Layer Meteorol., 149(1), 85–103, doi:10.1007/s10546-013-9834-x, 2013.

Schmitz, S.: XTurb-PSU: A Wind Turbine Design and Analysis Tool, [online] Available from: http://www.aero.psu.edu/Faculty_Staff/schmitz/XTurb/XTurb.html, 2012.

460   Sharma, V., Calaf, M., Lehning, M. and Parlange, M. B.: Time-adaptive wind turbine model for an LES framework, Wind Energy, 19(5), 939–952, doi:10.1002/we.1877, 2016.

Shin, H. H., Hong, S.-Y. and Dudhia, J.: Impacts of the Lowest Model Level Height on the Performance of Planetary Boundary Layer Parameterizations, Mon. Weather Rev., 140(2), 664–682, doi:10.1175/MWR-D-11-00027.1, 2011.

Skamarock, W. C. and Klemp, J. B.: A time-split nonhydrostatic atmospheric model for weather research and forecasting

465   applications, J. Comput. Phys., 227(7), 3465–3485, doi:10.1016/j.jcp.2007.01.037, 2008.

Stull, R. B.: An Introduction to Boundary Layer Meteorology, Springer., 1988.

Thompson, G. and Eidhammer, T.: A Study of Aerosol Impacts on Clouds and Precipitation Development in a Large Winter Cyclone, J. Atmos. Sci., 71(10), 3636–3658, doi:10.1175/JAS-D-13-0305.1, 2014.

Vanderwende, B. and Lundquist, J. K.: Could Crop Height Affect the Wind Resource at Agriculturally Productive Wind

470   Farm Sites?, Boundary-Layer Meteorol., 158(3), 409–428, doi:10.1007/s10546-015-0102-0, 2016.

Vanderwende, B. J., Lundquist, J. K., Rhodes, M. E., Takle, E. S. and Irvin, S. L.: Observing and Simulating the Summertime Low-Level Jet in Central Iowa, Mon. Weather Rev., 143(6), 2319–2336, doi:10.1175/MWR-D-14-00325.1, 2015.

Vanderwende, B. J., Kosović, B., Lundquist, J. K. and Mirocha, J. D.: Simulating effects of a wind turbine array using LES

475   and RANS, J. Adv. Model. Earth Syst., 8(3), 1376–1390, doi:10.1002/2016MS000652, 2016.

Vautard, R., Thais, F., Tobin, I., Bréon, F.-M., Lavergne, J.-G. D. de, Colette, A., Yiou, P. and Ruti, P. M.: Regional climate model simulations indicate limited climatic impacts by operational and planned European wind farms, Nat. Commun., 5, doi:10.1038/ncomms4196, 2014.

Volker, P. J. H., Badger, J., Hahmann, A. N. and Ott, S.: The Explicit Wake Parametrisation V1.0: a wind farm

480   parametrisation in the mesoscale model WRF, Geosci. Model Dev., 8(11), 3715–3731, doi:10.5194/gmd-8-3715-2015, 2015.

Wagner, R., Antoniou, I., Pedersen, S. M., Courtney, M. S. and Jørgensen, H. E.: The influence of the wind speed profile on wind turbine performance measurements, Wind Energy, 12(4), 348–362, doi:10.1002/we.297, 2009.

Wilczak, J., Finley, C., Freedman, J., Cline, J., Bianco, L., Olson, J., Djalalova, I., Sheridan, L., Ahlstrom, M., Manobianco, J., Zack, J., Carley, J. R., Benjamin, S., Coulter, R., Berg, L. K., Mirocha, J., Clawson, K., Natenberg, E. and Marquis, M.:

485   The Wind Forecast Improvement Project (WFIP): A Public–Private Partnership Addressing Wind Energy Forecast Needs, Bull. Am. Meteorol. Soc., 96(10), 1699–1718, doi:10.1175/BAMS-D-14-00107.1, 2015.

Wilczak, J. M., Oncley, S. P. and Stage, S. A.: Sonic Anemometer Tilt Correction Algorithms, Boundary-Layer Meteorol., 99(1), 127–150, doi:10.1023/A:1018966204465, 2001.

WRF-ARW: WRF Model Version 3.8: Updates, , doi:doi:10.5065/D6MK6B4K, 2016.

490   Wu, Y.-T. and Porté-Agel, F.: Large-Eddy Simulation of Wind-Turbine Wakes: Evaluation of Turbine Parametrisations, Boundary-Layer Meteorol., 138(3), 345–366, doi:10.1007/s10546-010-9569-x, 2011.
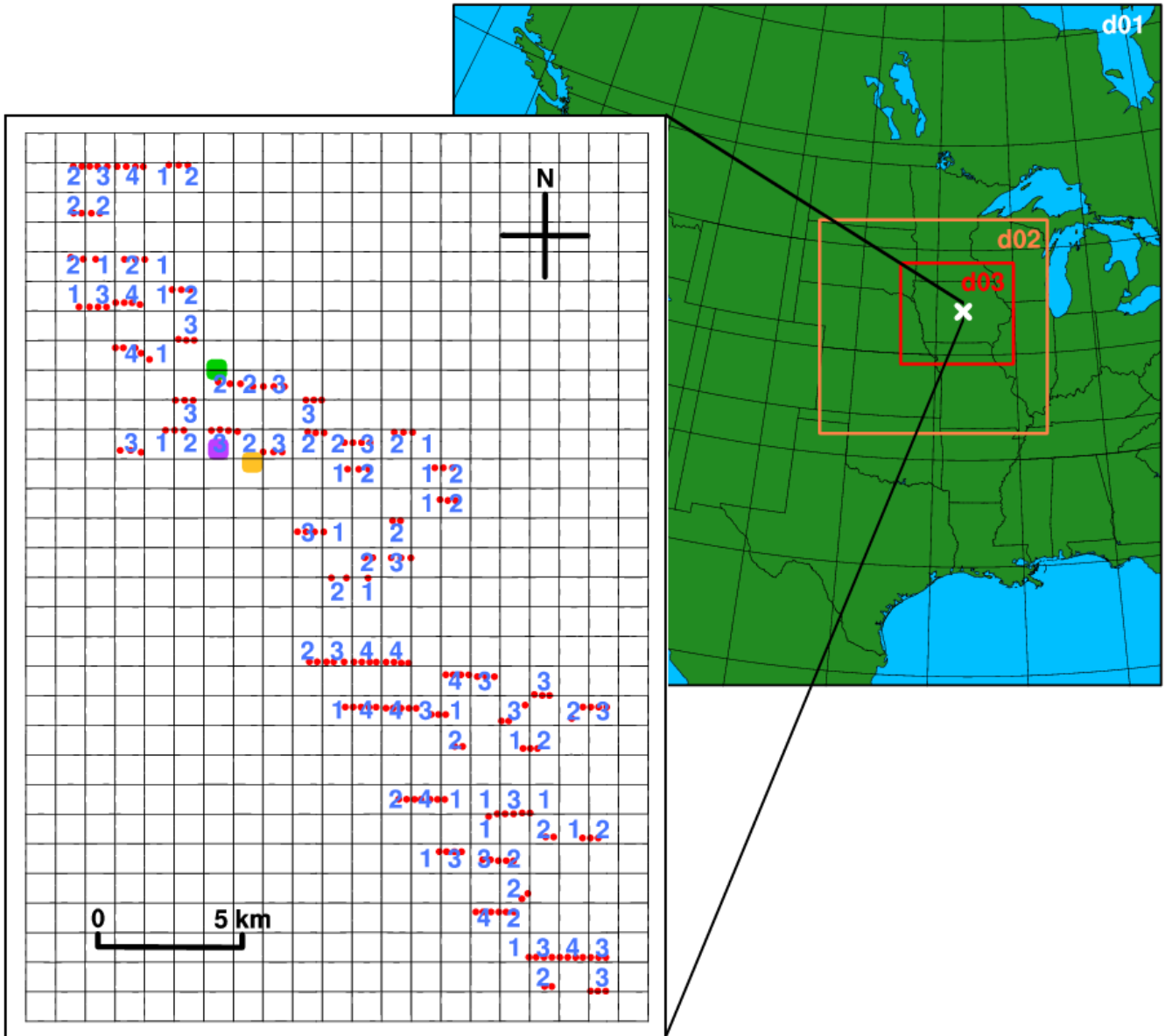
495

Figure 1: Map of the 3 domains (d01, d02 and d03) in the WRF simulations (right), with the white x representing the CWEX-13 wind farm. Zoom-in map of the wind farm (left), with the black horizontal and vertical lines outlining the WRF grid cells, the red dots as the actual locations of wind turbines, the blue numbers as the number of wind turbines per WRF grid cell, the yellow square as the WC lidar, the green square as the 200S lidar and the purple square as the surface flux station. Other instruments were deployed in CWEX-13, and only the instruments used herein are shown.

500
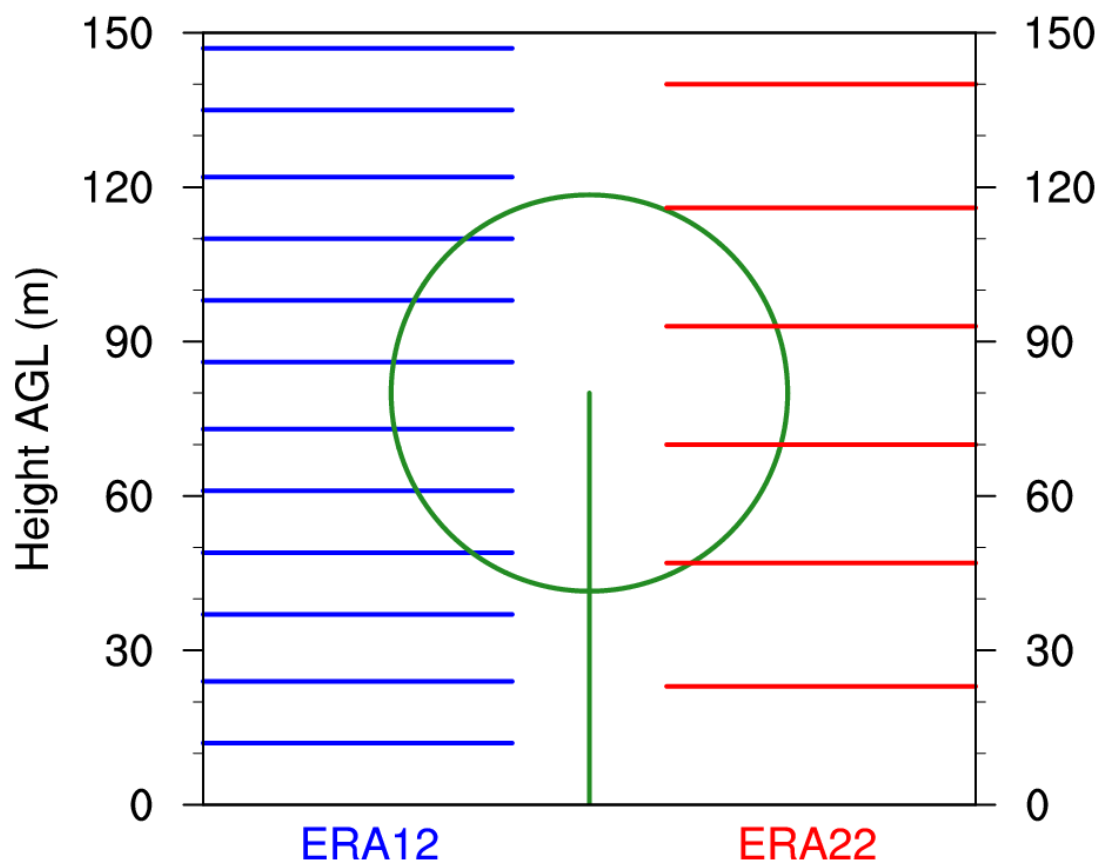
Figure 2: Illustration of the two vertical grids chosen: 12 m on the left in blue and 22 m on the right in red. Both grids shown use the ERA-interim as the boundary conditions. The simulations initiated with the 0.5° GFS have slightly different grids.
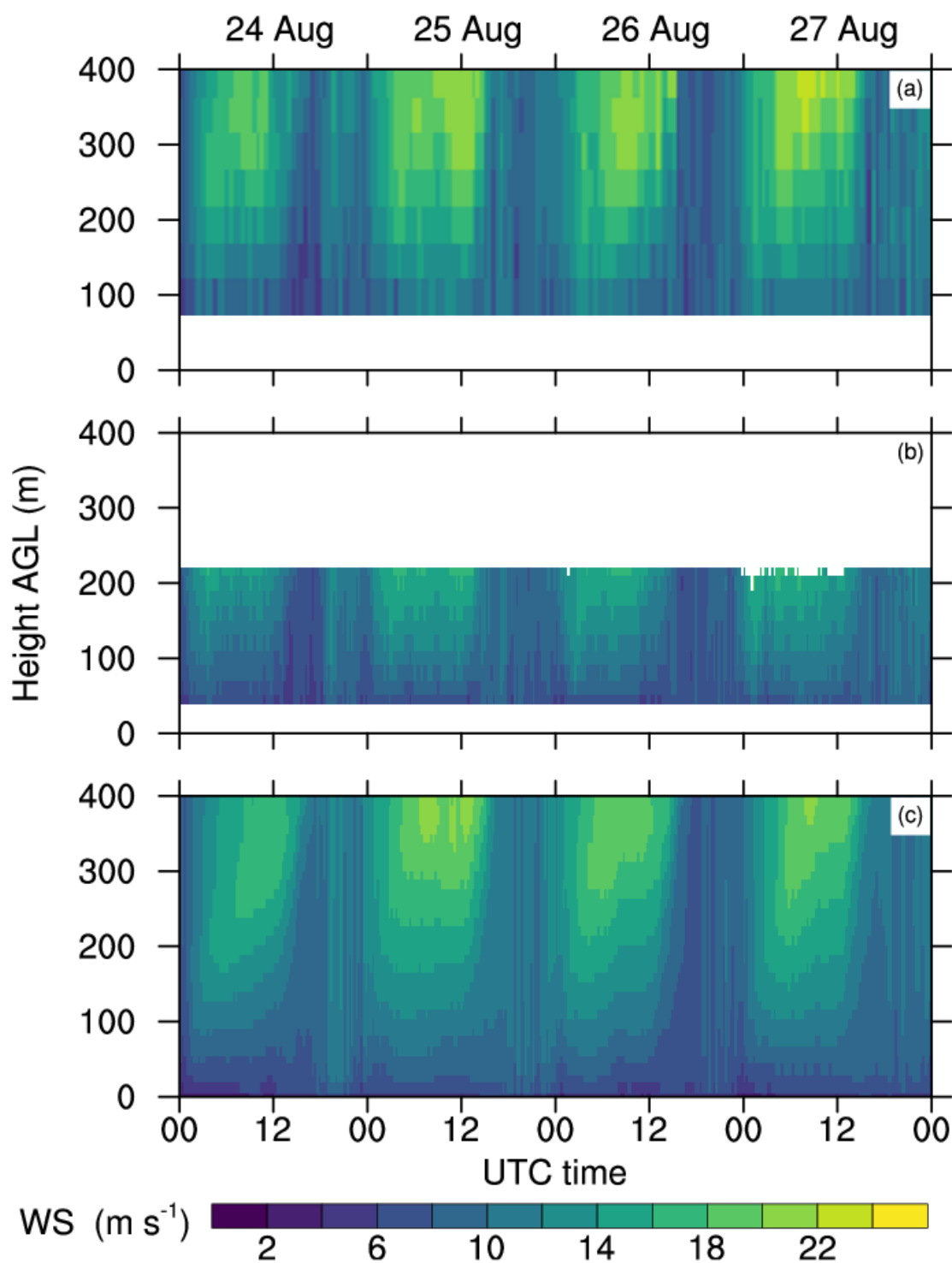
505

Figure 3: Time-height contour of WS from the 200S (a), the WC (b) and ERA12 at the closest grid point to the 200S (c).
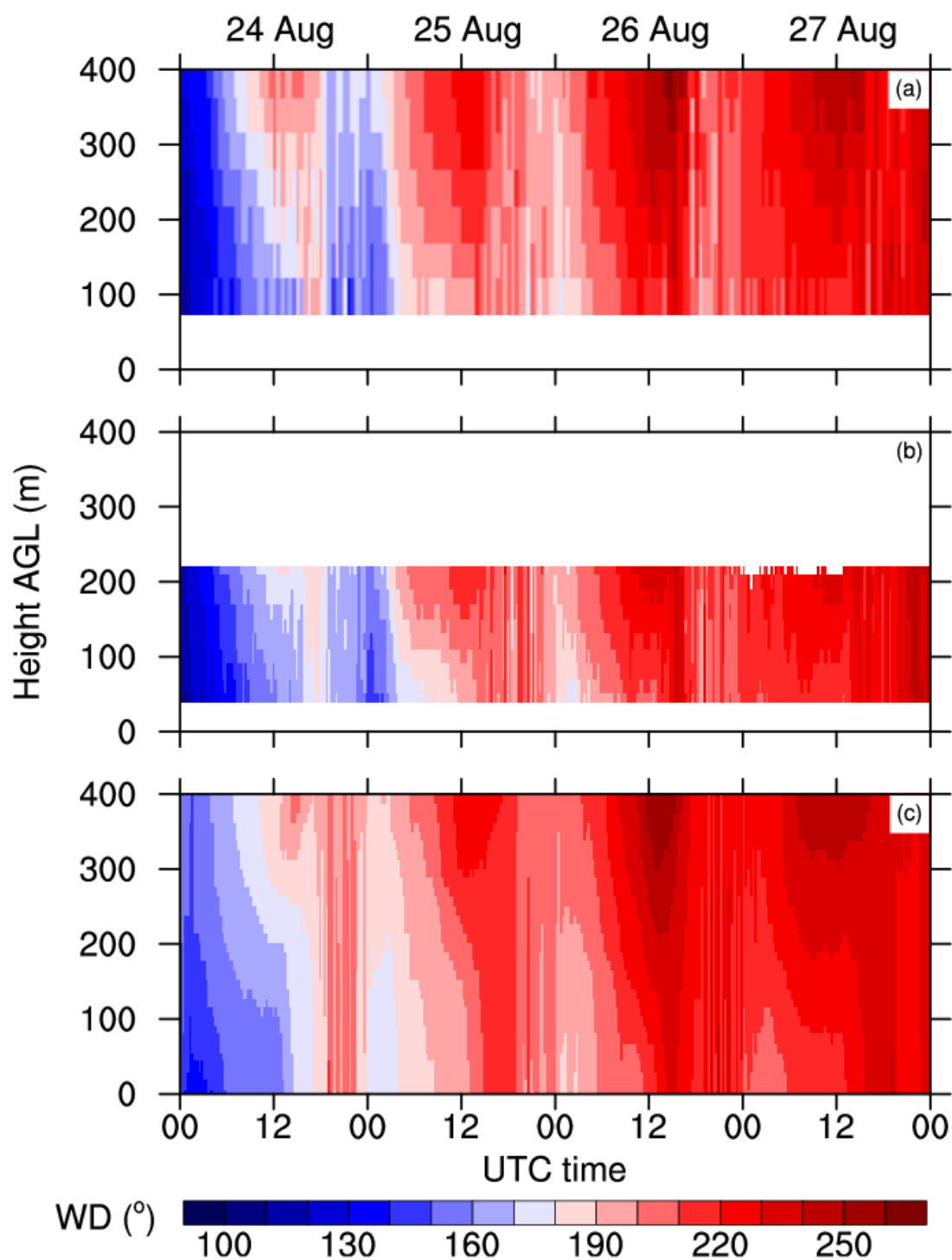
Figure 4: As in Fig. 3, but for WD.
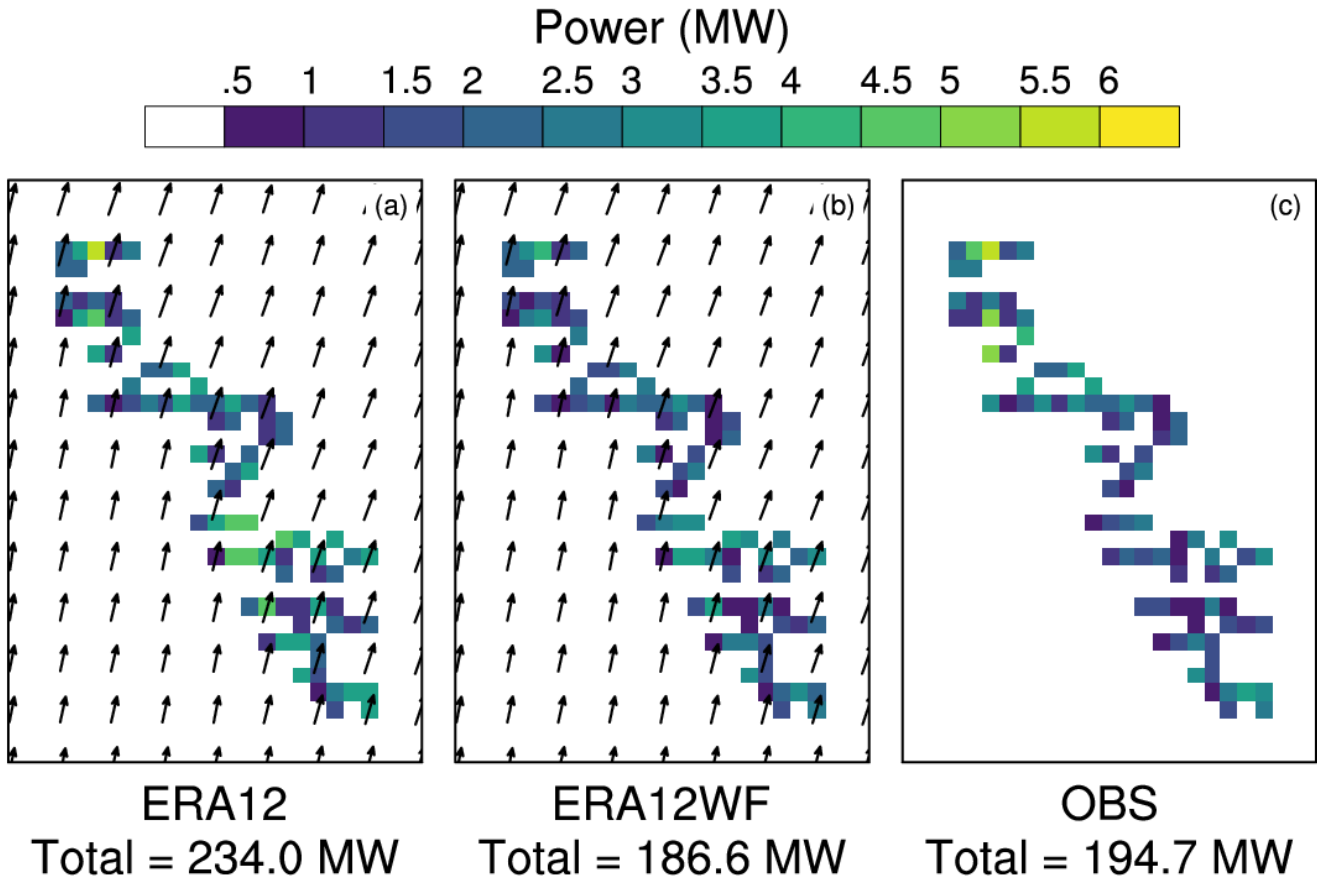
510

Figure 5: The power production for one 10-min period from the ERA12 estimates (a), the ERA12WF outputs (b) and the observation (abbreviated as OBS) (c). The total power in each grid cell is presented regardless of the number of turbines in each cell, and the wind-farm totals are summarized at the bottom. The vectors indicate the simulated winds, and their lengths correspond to the horizontal velocity magnitude.

515
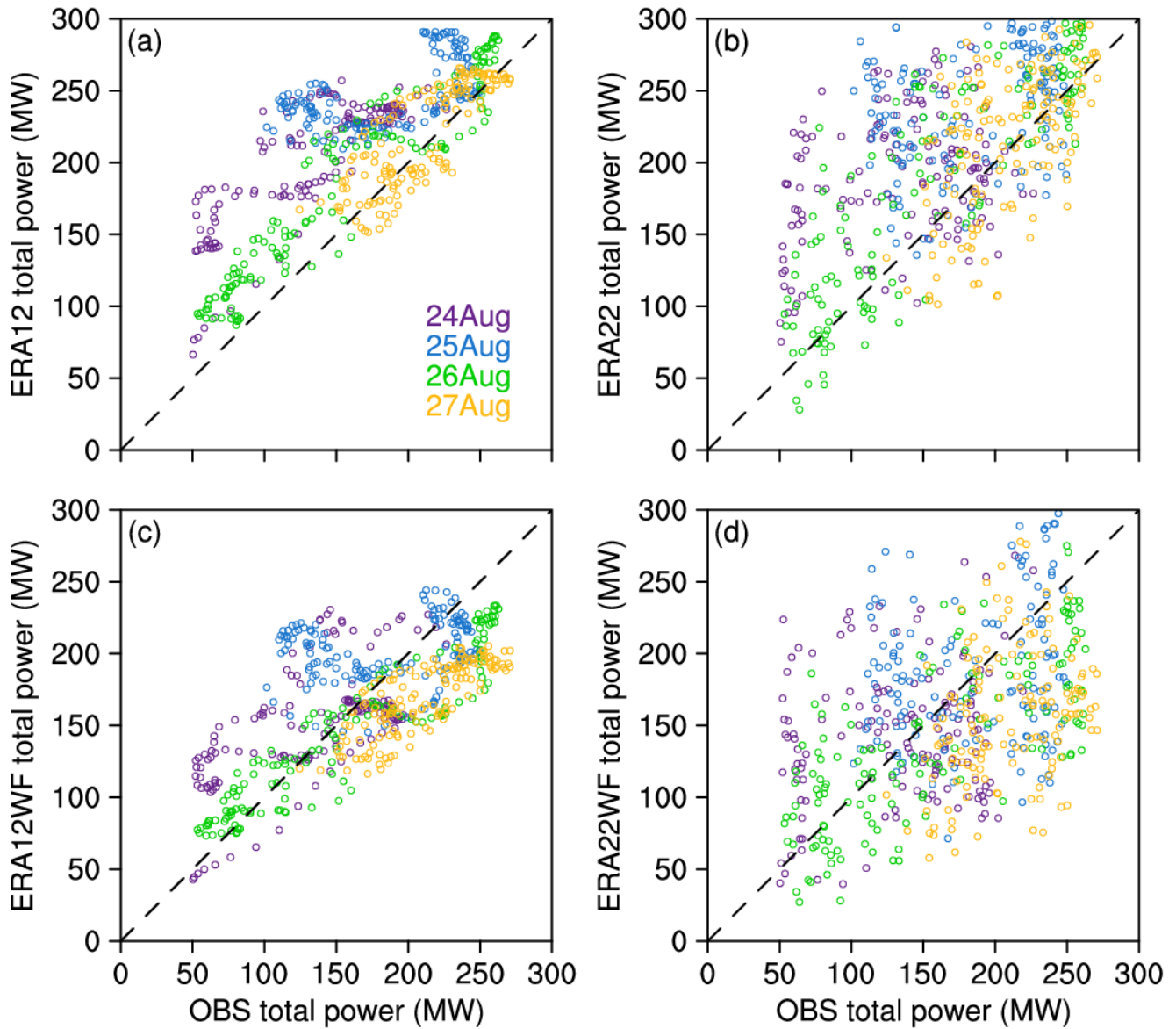
Figure 6: Scatter plots comparing the 10-min average observed total power against the calculated total power from the ERA12 (a) and the ERA22 (b), and the simulated total power from the ERA12WF (c) and the ERA22WF (d). The dots represent the total power on 24 August (purple), 25 August (blue), 26 August (green) and 27 August (yellow).

520
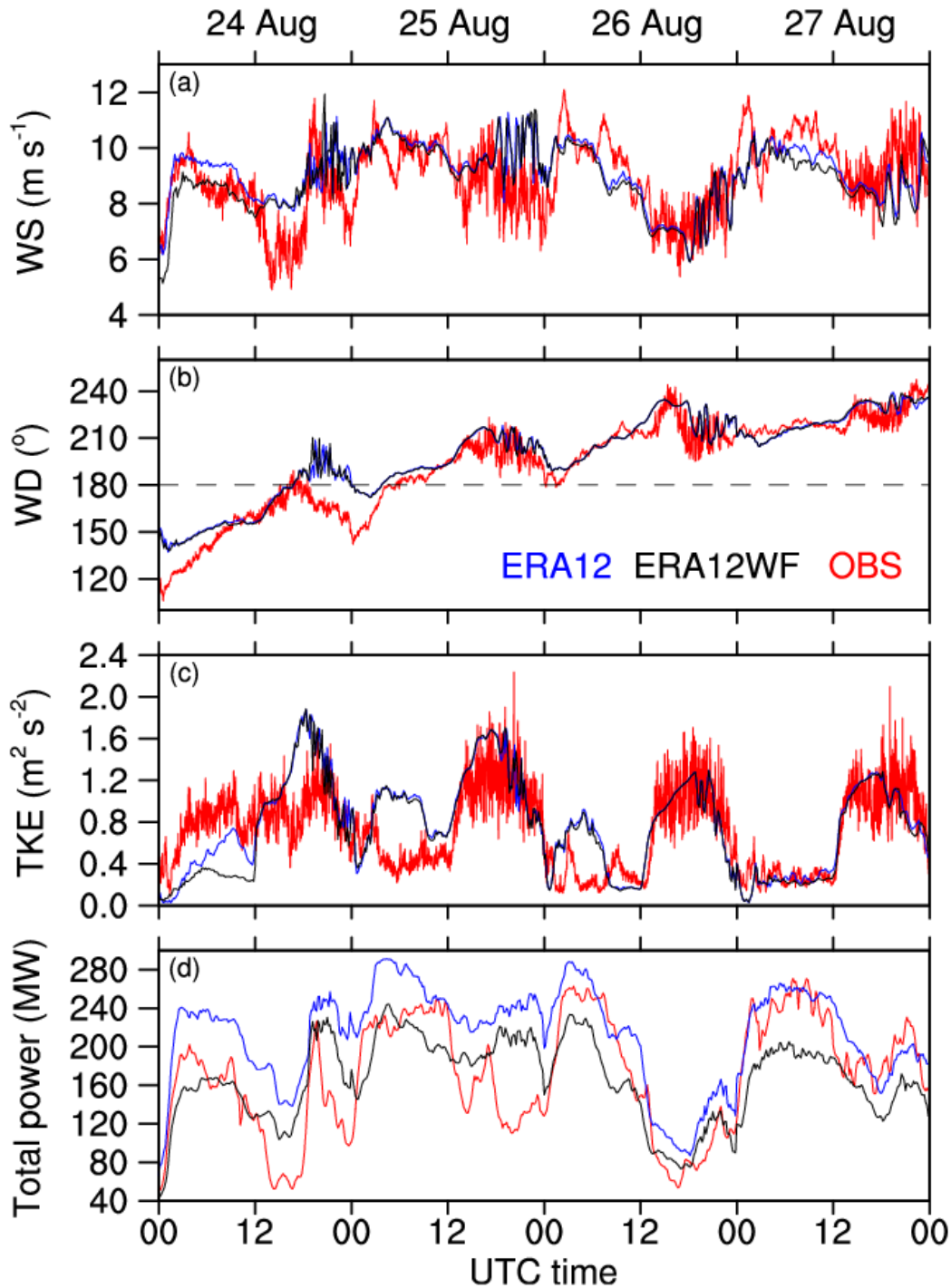
Figure 7: Time series of hub-height WS (a), hub-height WD (b), hub-height TKE (c), and total wind farm power (d) from the WC measurements (in red) and the simulations (ERA12WF, in black; ERA12, in blue). The simulated values are interpolated to hub height at the grid point closest to the WC location. In (b), the grey horizontal dash line marks the WD of 180°.
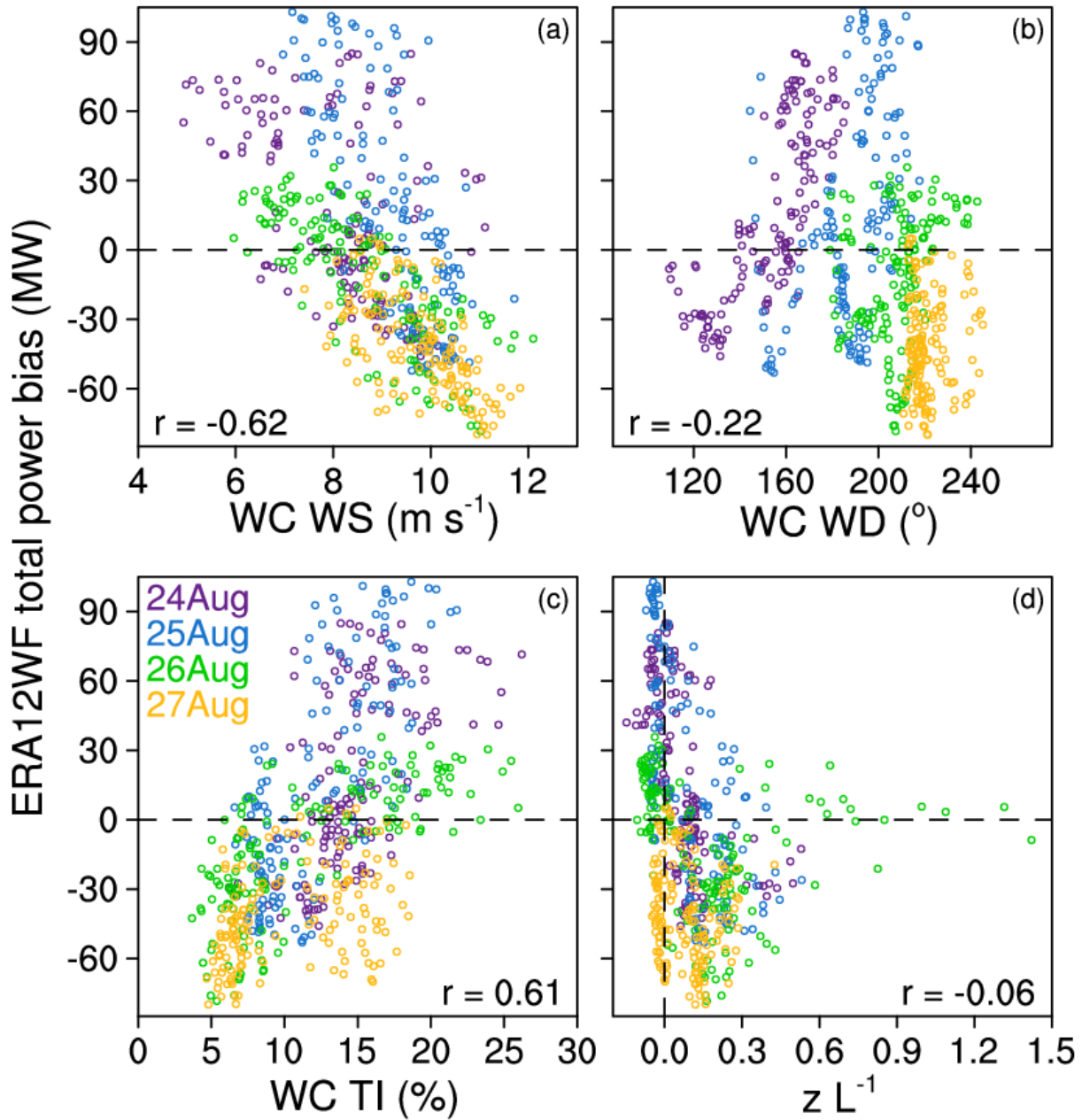
525

Figure 8: Scatter plots comparing the bias of the ERA12WF 10-min total power to the WC-observed hub-height WS (a), hub-height WD (b), hub-height TI (c) and stability parameter z L⁻¹ measured at the surface flux station (d). The r represents the Pearson correlation coefficient. Similar to Fig. 6, different coloured dots represent biases on different days. The horizontal black dash lines mark the zero power bias, and the vertical black dash line in (d) at zero z L⁻¹ differentiates the two stability regimes.
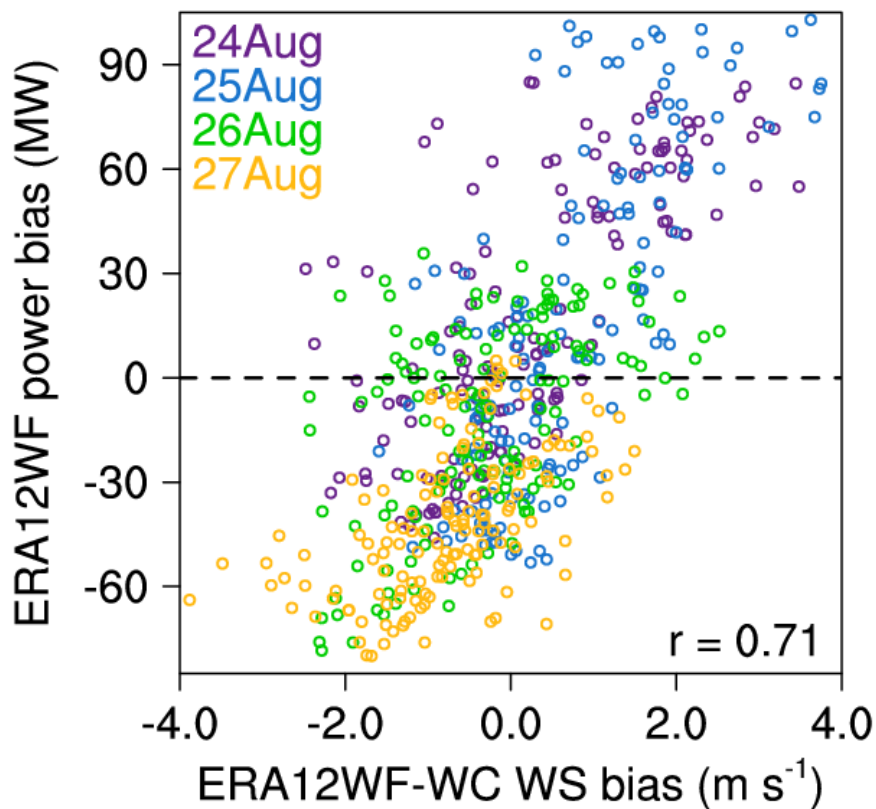
530

Figure 9: Scatter plot between the bias of the ERA12WF 10-min total power compared to observation, and its bias of the simulated hub-height WS in the closest grid cell to the WC. The r represents the Pearson correlation coefficient.
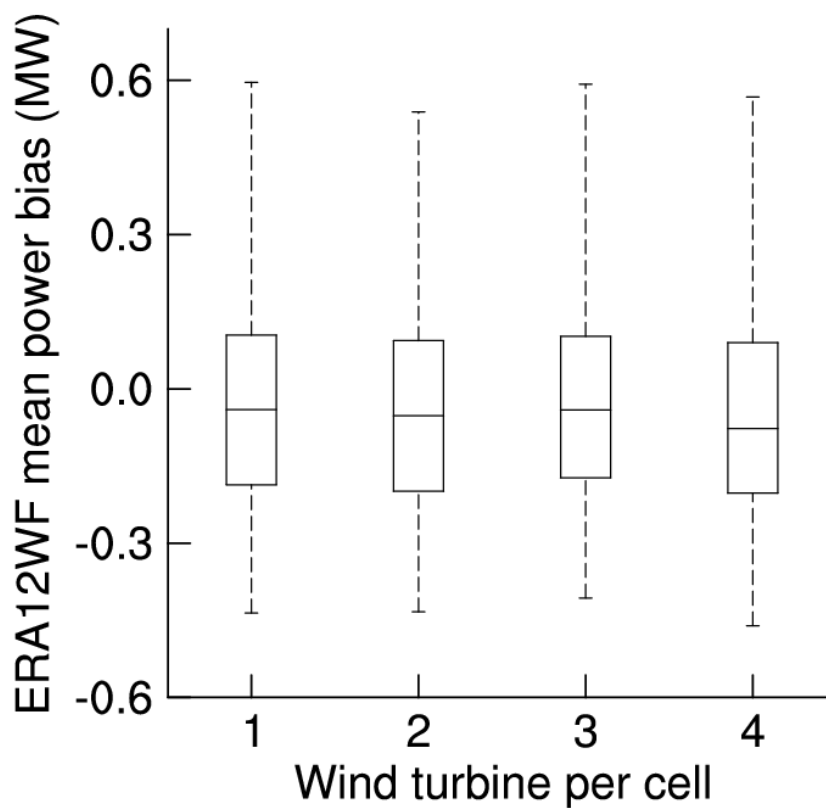
535   **Figure 10: Boxplot of the average bias of the ERA12WF simulated power across different numbers of wind turbine per WRF grid cell every 10 minutes during the 4-day period.**
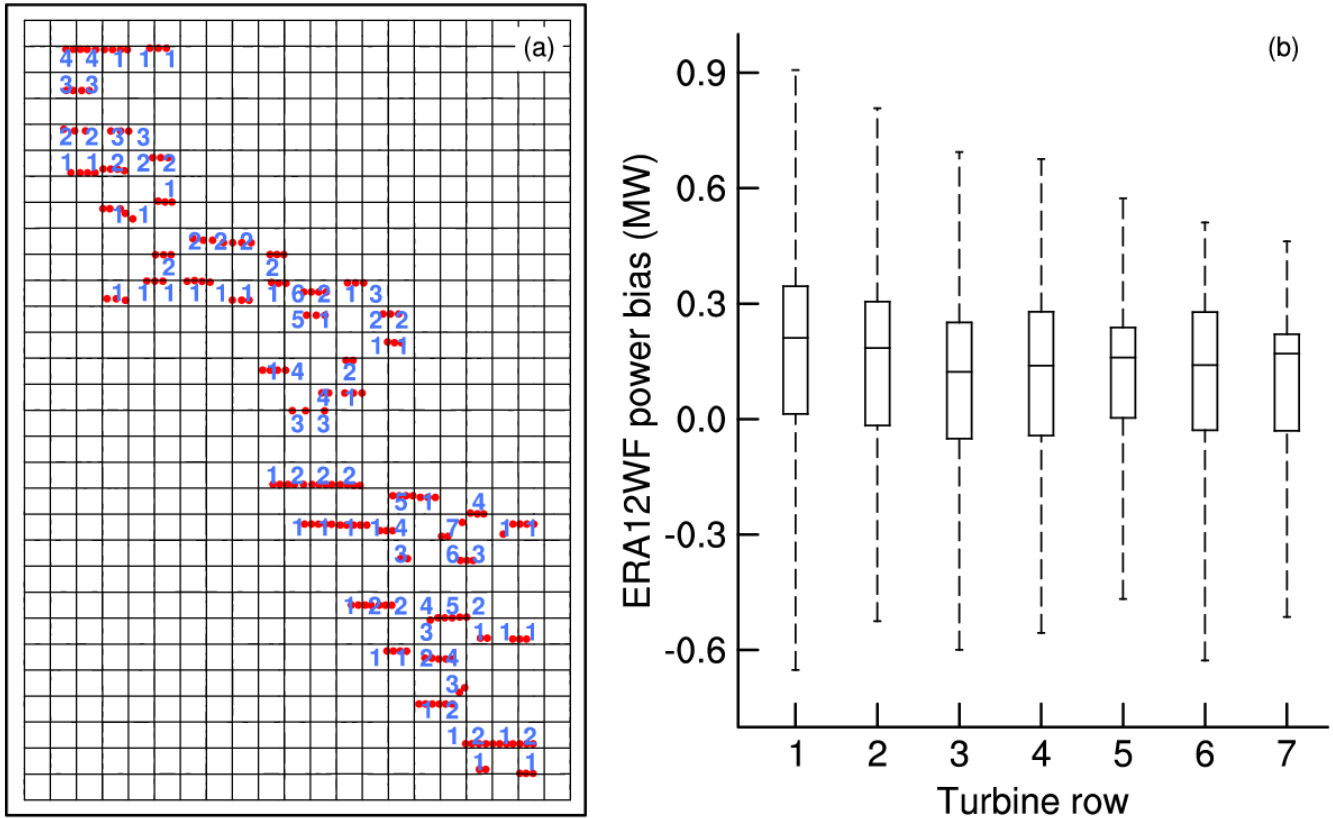
Figure 11: Map of the wind farm where the blue numbers represent the row number from the upwind row during southerly winds
540 **(a). The upwind row number is reset to 1 when the next two downwind grid boxes to the North contain no turbines. Boxplot of the average ERA12WF power bias normalized over different number of wind turbine rows, when the hub-height WD in the grid cell closest to the WC is between 175° to 185° (b).**

545 **Table 1: The WRF model configuration.**

Parameterization	Scheme	Reference
Cumulus	Kain-Fritsch	Kain (2004)
Land surface	NOAH LSM	Ek et al. (2003)
Land surface roughness	Thermal roughness length	Chen and Zhang (2009)
Microphysics	Thompson aerosol-aware	Thompson and Eidhammer (2014)
PBL	MYNN Level 2.5	Nakanishi and Niino (2006)
Radiation	RRTMG	Iacono et al. (2008)

Table 2: List of WRF simulations and their features.

Run name	Boundary condition	Vertical resolution	WFP
ERA12	ERA-interim	12 m	No
ERA22	ERA-interim	22 m	No
GFS12	0.5° GFS	12 m	No
GFS22	0.5° GFS	22 m	No
ERA12WF	ERA-interim	12 m	Yes
ERA22WF	ERA-interim	22 m	Yes
GFS12WF	0.5° GFS	12 m	Yes
GFS22WF	0.5° GFS	22 m	Yes

550 **Table 3: Average absolute error in WS (m s⁻¹) and WD (°) of different no-WFP runs.**

	ERA12	ERA22	GFS12	GFS22
200S 120 m WS	1.49	1.84	**1.35**	1.54
WC 120 m WS	**1.21**	1.63	1.34	1.48
WC 80 m WS	**1.24**	1.64	1.36	1.55
WC 40 m WS	**1.47**	1.9	1.53	1.86
200S 120 m WD	14.99	15.98	**14.68**	14.99
WC 120 m WD	**12.66**	13.86	13.07	13.47
WC 80 m WD	**13.23**	14.55	13.85	14.24
WC 40 m WD	**14.19**	15.58	14.83	15.15

The smallest errors across different WRF settings are highlighted in bold.

555 **Table 4: RMSE of 10-min total power (MW) of different model runs each day.**

	24 Aug	25 Aug	26 Aug	27 Aug	4-day mean
ERA12	73.6	73.5	**35.4**	**22.6**	**51.3**
ERA22	79.5	**72.8**	48.5	41	60.5
GFS12	**62**	76.5	58.3	40.9	59.4
GFS22	73.9	89.6	65.3	51.9	70.2
ERA12WF	42.2	**49.4**	**31.1**	46.5	**42.3**
ERA22WF	61.7	61.2	50.9	71.6	61.4
GFS12WF	46.2	54.6	34.1	**36.1**	42.8
GFS22WF	**40**	60	32.6	37.3	42.5

Table 5: Average bias of 10-min total power (MW) of different model runs each day.

	24 Aug	25 Aug	26 Aug	27 Aug	4-day mean
ERA12	68.3	62.6	**26.8**	8.1	41.5
ERA22	58.3	**52.1**	28	**6.2**	**36.2**
GFS12	**49.4**	65	51.8	29	48.8
GFS22	65.5	80.7	60.3	35.8	60.6
ERA12WF	17.5	16.6	-12.2	-41.6	-4.9
ERA22WF	10.4	**0.6**	-17.6	-53.6	-15.1
GFS12WF	3.8	22.2	**9.6**	-18.6	**4.3**
GFS22WF	**2.9**	29.7	10.9	**-12.3**	7.8

The RMSEs and biases closest to zero across different days are highlighted in bold.

560

Table 6: Differences (first value) and p-values (second value) from 2-sample t-tests of simulated power from different ERA runs.

		ERA12	ERA12WF	ERA22WF
	4-day mean	41.8	-4.9	-15.1
ERA12	41.9		-46.8; 0	
ERA22	36.1	5.7; 0.0300		-51.2; 0
ERA12WF	-4.9			
ERA22WF	-15.1		10.2; 9.60×10^{-4}	

Table 7: As in Table 6, but for GFS runs.

		GFS12	GFS12WF	GFS22WF
	4-day mean	48.6	4.2	7.8
GFS12	48.6		-44.4; 0	
GFS22	60.6	-12.0; 1.09×10^{-7}		-52.8; 0
GFS12WF	4.2			
GFS22WF	7.8		-3.6; 0.163	

565

Table 8: P-values from 2-sample t-tests of the 10-min observed power and the 10-min simulated power from different model runs.

	Simulated 4-day mean	Observed 4-day mean	Difference of means	P-value
ERA12	212.7		41.8	0
ERA22	207.0		36.1	0
GFS12	219.5		48.6	0
GFS22	231.4	170.9	60.5	0
ERA12WF	166.0		-4.9	0.106
ERA22WF	155.8		-15.1	6.54×10^{-6}
GFS12WF	175.1		4.2	0.167
GFS22WF	178.7		7.8	0.0136